

## Aerodynamic Fragmentation of Drops: Dynamics of the Liquid Bag

L. Opfer<sup>\*,1</sup>, I. V. Roisman<sup>1,2</sup>, C. Tropea<sup>1,2</sup>

<sup>1</sup>Institute of Fluid Mechanics and Aerodynamics, Technische Universität Darmstadt, Germany

<sup>2</sup>Center of Smart Interfaces, Technische Universität Darmstadt, Germany

lopf@sla.tu-darmstadt.de, roisman@sla.tu-darmstadt.de and ctropea@sla.tu-darmstadt.de

### Abstract

This study is devoted to the experimental and theoretical investigation of aerodynamic bag breakup phenomena. While the qualitative development and morphology of single bag breakup events is well understood, the exact physics that lead to deformation and breakup of the drops are still unclear. Especially the mechanism that leads to bursting of the bag is not understood up to now. A compact open-circuit wind tunnel has been designed in order to conduct the experiments. A high-speed video system is used for shadowgraph visualizations with high temporal and spatial resolution. The experiments are carried out for various Weber numbers. A qualitative analysis of the breakup evolution is performed by means of digital image processing. Algorithms are developed in order to track the leading and trailing side of the drop and growth of the liquid bag. A new theoretical model is presented which describes the dynamics of the liquid bag. The governing equations of the bag motion are solved taking into account for the aerodynamic pressure, inertia and surface tension in the liquid bag. It is shown that the model predictions agree well with the experimental results.

---

### Introduction

Once a drop is exposed to a gaseous environment that moves with a relative velocity, the surface of the drop is subject to aerodynamic forces. These aerodynamic forces are responsible for acceleration and deformation of the drop and may finally lead to disintegration when the relative velocity exceeds a certain limit.

The aerodynamic breakup of drops and ligaments is one of the most important phenomena responsible for the atomization of bulk liquid into single fragments. It is responsible for the final spray characteristics in a variety of technical applications and everyday phenomena, such as: fuel injection in jet engines [1, 2] and internal combustion engines, paint deposition, wire-arc coating [3] and rain [4].

Due to its importance the aerodynamic fragmentation has been interest of research for some decades. Recent comprehensive reviews about this topic can be found in [5] and [6].

The ratio between deforming aerodynamic forces and restoring surface tension forces is described by the gas Weber number:

$$We = \frac{\rho_a D_0 U^2}{\sigma}, \quad (1)$$

where  $\rho_a$  is the gas density,  $D_0$  is the initial drop diameter,  $U$  is the relative velocity between liquid and gas phase and  $\sigma$  is the surface tension coefficient.

Depending on the Weber number, different deformation and breakup modes have been identified in the literature. One of the most common classifications of the aerodynamic breakup regimes is given by Hsiang and Faeth [7]:

- vibrational deformation and breakup ( $We < 11$ )
- bag breakup ( $11 > We < 25$ )
- multimode breakup ( $25 < We < 80$ )
- shear breakup ( $We > 80$ ),

while a similar classification can be found in [8]. The transition Weber numbers shown above are valid for low viscosity liquids. More recently, another classification is given by Theofanous and Li [9] that groups all breakup modes in two main regimes, *Rayleigh-Taylor piercing (RTP)* and *shear-induced entrainment (SIE)*.

There exist two different approaches for the experimental investigation of aerodynamic fragmentation. Breakup experiments can be conducted in a continuous gas flow, as done in [10]. The second experimental approach is the

---

\*Corresponding author: lopf@sla.tu-darmstadt.de

employment of a shock tube, as used in [11]. While shock tube experiments are more intricate, the use of such a device avoids the problem that the the drop has to pass through a boundary layer before it enters the homogeneous flow field.

The most commonly used technique for the experimental investigation of aerodynamic fragmentation is the shadowgraph visualization. The availability of digital high-speed cameras during the last decade revealed quantitative, time-resolved information about the breakup processes. In [12] Laser Induced Fluorescence is used to visualize not only the contour of the drop but the structure of the liquid surface during the fragmentation. The authors conclude that pure shadowgraph visualizations might lead to misinterpretations concerning the physics of high  $We$  breakup events.

Flock et al. [13] successfully used Particle Image Velocimetry in order to measure velocity fields in the gas phase around the fragmenting drop in the bag and shear breakup regime. Their results also reveal quantitative information about the backflow in the wake of the drop.

Among the fragmentation regimes described above, the bag and multimode breakup are the dominant fragmentation modes for most applications, since they occur at relatively low Weber numbers. While the qualitative development and morphology of single bag breakup events is well understood, the exact physics that lead to deformation and breakup of the drops are still unclear. Especially the mechanism that leads to bursting of the bag is not understood up to now. This study is devoted to the further experimental and theoretical investigation of bag breakup phenomena at low Weber numbers.

## Experimental Methods & Data Processing

### Experimental Setup

A compact, open-circuit wind tunnel has been designed and manufactured for the experimental investigation of drop deformation and breakup under crossflow conditions. A sketch of this windtunnel is depicted in figure 1.

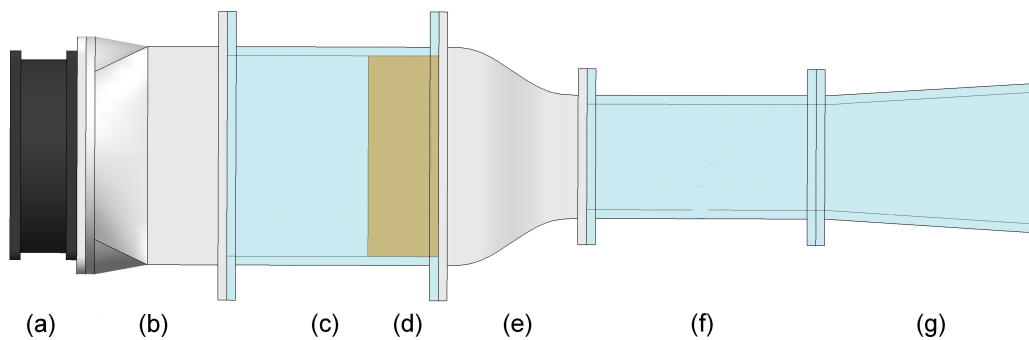


**Figure 1.** Windtunnel used for the experiments.

The air is driven by an axial blower (a). The blower is connected to the settling chamber (c) by an adapter (b), which continuously transforms the round cross-section of the blower to the square cross-section of the windtunnel. The cross-sectional area of the settling chamber is  $120 \times 120 \text{ mm}^2$ . The air is led through a honeycomb structure (d) in order to straighten the flow and to suppress vortices above a certain size. The airflow is then accelerated into the test section (f) by a nozzle (e). The cross-sectional dimensions of the test section are  $60 \times 60 \text{ mm}^2$ . This gives a nozzle contraction ratio of 4. The air is then decelerated in a diffuser (g) to reduce the pressure loss at the outlet into the ambient air.

The settling chamber, test section and the diffuser are manufactured from transparent acrylic glass. This provides good optical access into the complete test section, so that no additional windows have to be installed. The more complex geometries of the adapter and the nozzle are manufactured in a rapid prototyping machine from polyamide.

Drops are produced by a syringe and are accelerated into the test section by gravity. However, the drops are exposed to the boundary layer at the upper wall of the windtunnel when entering the flow field. This leads to an asymmetric deformation of the drop inside the boundary layer. To overcome this problem, the drops are injected into the crossflow through a symmetric airfoil (Eppler 168). The airfoil protects the drops from the wall boundary layer and enables them to fall freely into the homogeneous core of the velocity profile. The drops are then exposed to the boundary layer of the the airfoil itself, which is very small compared to the wall boundary layer of the wind tunnel. A sketch of the test section is shown in figure 2

The rotational speed of the axial blower that drives the windtunnel can be variably controlled by a potentiome-

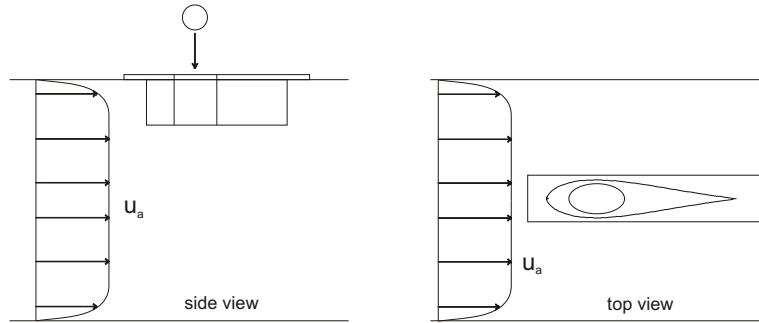


**Figure 2.** Sketch of the test section and the airfoil used for shielding the drop from the wall boundary layer.

Exp. No.	liquid	$D_0$ [mm]	$\rho_l$ [kg/m <sup>3</sup> ]	$\sigma$ [N/m]	$U_a$ [m/s]	$We$ [-]
1	isopropanol	1.82	780	21.2e-3	10	8.6
2	water	2.98	1000	73e-3	15	9.2
3	isopropanol	2.26	780	21.2e-3	10	10.6
4	water	3.51	1000	73e-3	15	10.8

**Table 1.** Overview of the experimental parameters considered in this study.

ter. That allows an adjustment of the air velocity in the test section between 0 and 30 m/s. A Pitot tube and a *Setra* 239 differential pressure sensor are used to determine the air velocity.

A *Vision Research Phantom V12* high speed camera is used to record time resolved shadowgraph images of the drop deformation and breakup process. The camera is operated at a framerate of 7900 images per second and a resolution of  $1024 \times 768$  pixel. A 50 mm *ZEISS* lens is employed that gives a spatial resolution of  $46 \mu\text{m}/\text{pixel}$ . The sensor of the camera is illuminated by a continuous mercury vapor lamp.

### Image Processing

An image processing algorithm is developed in order to quantitatively analyze the recorded shadowgraphs. The algorithm is implemented in *Matlab*. First, a reference image is subtracted from each frame. This removes the influence of inhomogeneous illumination. Then, the algorithm recognizes and tracks the drop while being exposed to the crossflow. The instantaneous position of the drop as well as its extent in the airflow direction and perpendicular to that are determined for each time step.

The algorithm is able to recognize the drop shape with an uncertainty of two pixels on each side of the drop. For the given optical configuration the size of the spherical or mildly deformed drop on the camera sensor is around 100 pixel. That gives an uncertainty in the length measurements of about 4%. However, once the drop is inflated by the airflow its size on the sensor rapidly increases to several hundred pixels. The uncertainty then decreases to well below one percent.

### Results and Discussion

The typical evolution of a single bag breakup event is shown in figure 3. Once the undisturbed drop (3(a)) is exposed to the airflow, it is deformed (3(b)) until it takes the shape of a disc (3(c)). After that, the first occurrence of the liquid bag can be observed (3(d)). The liquid bag then grows due to the stagnation pressure inside (3(e) and 3(f)). This growth continues until the liquid film suddenly bursts (3(g)). The rupture of the liquid film initiates the disintegration of the liquid film, leaving behind a liquid torus. This rim itself is not stable and is fragmented by RT-instabilities.

A bimodal drop size distribution is the typical outcome of such a Bag breakup. The first peak of the distribution is governed by the very small drops that result from the disintegration of the liquid film that forms the bag. The typical size of these small drops directly depends on the thickness of this liquid film. The second peak represents

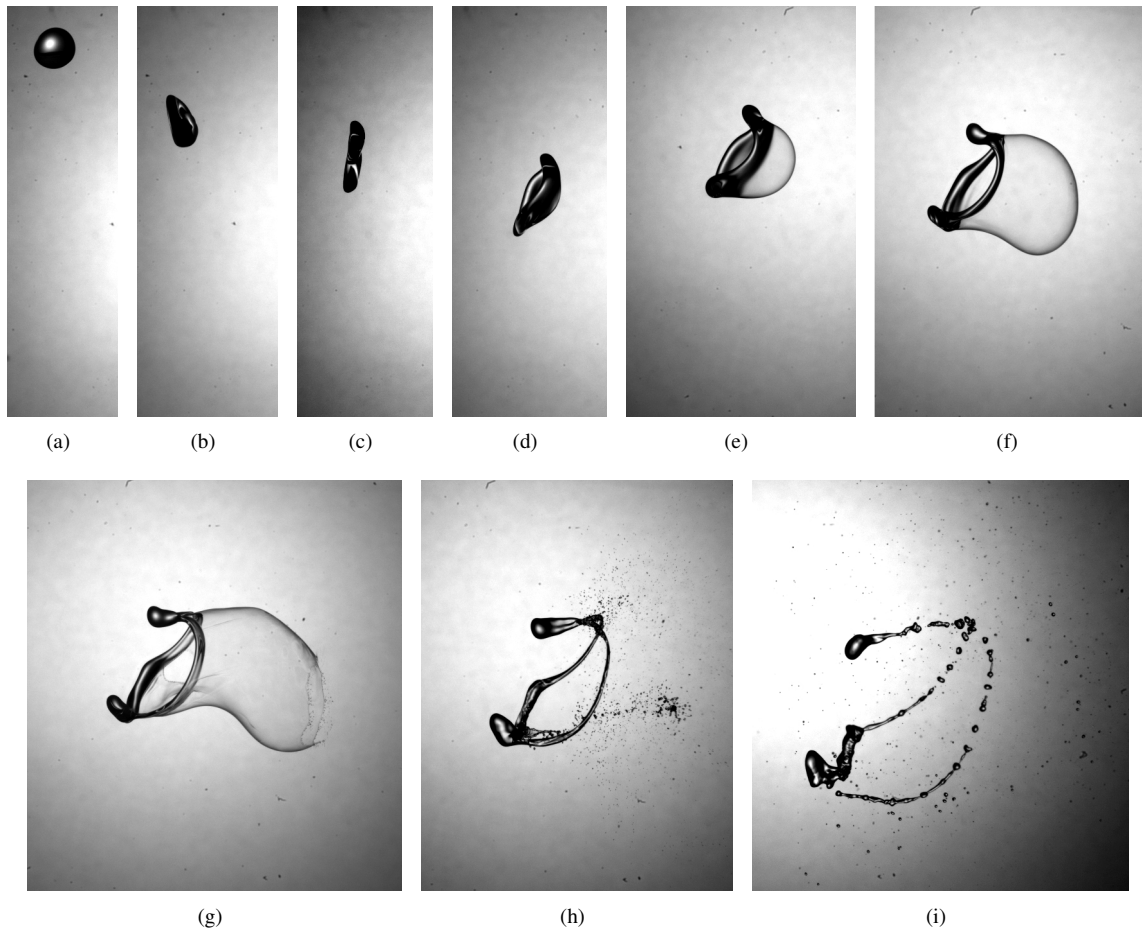


**Figure 3.** Typical evolution of a single bag breakup.

the much larger drops that are formed by the RT-instability on the rim. Their typical diameter is dominated by the fastest growing wavelength of the instability and both diameters of the toroid. However, the dimensions of the rim as well as the film thickness of the bag are strongly changing with time. The final outcome of a single breakup event is thus dominated by the dynamics of the bag and the rim.

An illustration of the variables used for description of the liquid bag dynamics is given in Figure 4. Figure 5 depicts the temporal evolution of the drop length  $L$  and radius  $R$  for various Weber numbers. The time is made non-dimensional by  $T = tU_a/D_0\epsilon^{-1/2}$ , where  $t$  is time and  $U_a$  is the air velocity.  $\epsilon$  is the density ratio  $\rho_l/\rho_a$ , where the subscript  $l$  refers to the liquid phase and the subscript  $a$  refers to the gas phase (air).

The length  $L$  (Fig. 5(a)) first decreases in all experiments until it reaches a minimum. In this initial stage, the drop is deformed by the airflow and the spherical shape of the undisturbed drop is transformed to a disc shape.

The pressure difference between the front and the rear side of the drop causes the middle of the disc to bulge. The length of the drop increases again with the growing bag. The growth rate of the liquid bag increases with increasing  $We$ . This can be explained by the weaker influence of surface tension that opposes deformation of the drop. It is interesting to note how clearly the effect of small differences in  $We$  can be observed in the results.

The results show that the liquid bag typically bursts when the non-dimensional length  $L/D_0$  of the drop is between four and six. Once the bag has burst, surface tension causes the liquid film to retract and  $L/D_0$  rapidly decreases. The time of rupture can thus clearly be identified from the data by finding the maximum value of  $L$ . The timespan between the minimum and the maximum of  $L$  can be used as typical breakup time. Since both peaks of  $L/D_0$  are very distinct, this timespan can be evaluated automatically.

The temporal evolution of the drop radius is shown in figure 5(b). The radius increases monotonically with time. A sharp bend can be observed in all cases at  $T \approx 2$ . This indicates that the radius of the bag grows faster than the radius of the rim (see Fig. 3(e) and 3(f)).

The downstream position of the drop tip  $H$  is depicted in figure 6. During the initial deformation stage, the

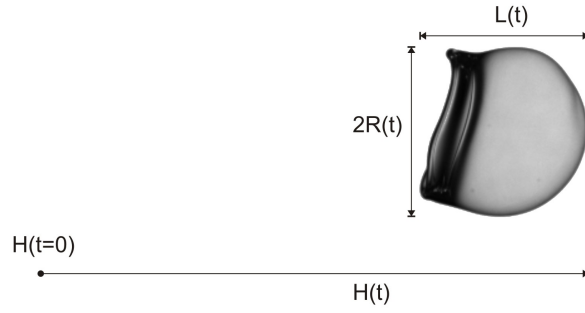


**Figure 4.** Definition of the variables

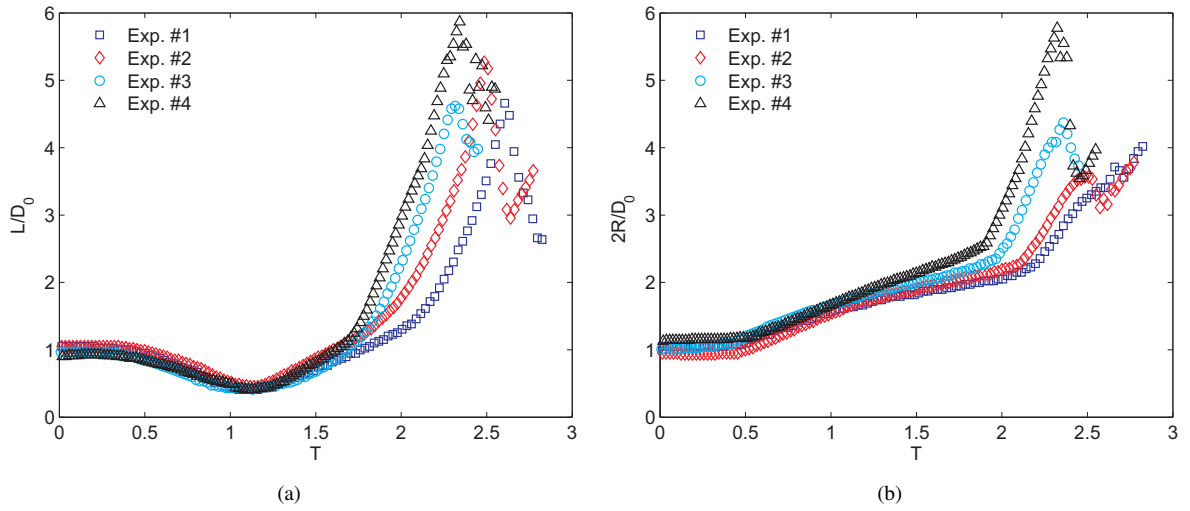


**Figure 5.** Results from the measurements of drop length  $L$  and drop radius  $R$ .

tip position remains almost constant, while the overall drop shape is heavily altered by the airflow. A significant motion of the tip starts once the deformation stage is completed and the drop has taken disc shape. Again, the tip velocity correlates with the Weber number of the corresponding drop. Larger  $We$  leads to higher tip velocities.

## Theoretical Modeling

### Initial drop deformation

Consider initial drop deformation under the action of the aerodynamic pressure associated with the air flow. We approximate the deformed drop by a cylinder of radius  $R(t)$ . The aerodynamic pressure at the stagnation point can be evaluated using the stationary Bernoulli equation,  $p_0 \approx \rho_a U_a^2 / 2$ , since the nonstationary terms associated with the acceleration and shape change are negligibly small. On the other hand, the pressure at the edge  $r = R(t)$  reverts to the static pressure (taken as zero). The pressure distribution can be estimated by a parabolic profile

$$p = p_0 \left( 1 - \frac{r^2}{R^2(t)} \right). \quad (2)$$

Assuming a linear velocity distribution of the liquid flow in the cylinder,  $v_r = r\dot{R}/R$  in the momentum balance equation in the radial direction

$$\rho_l (v_{r,t} + v_r v_{r,r}) + p_{,r} = 0, \quad (3)$$

where the second subscript denotes differentiation, yields:

$$\ddot{R}R = \frac{\rho_a}{\rho_l} U_a^2. \quad (4)$$

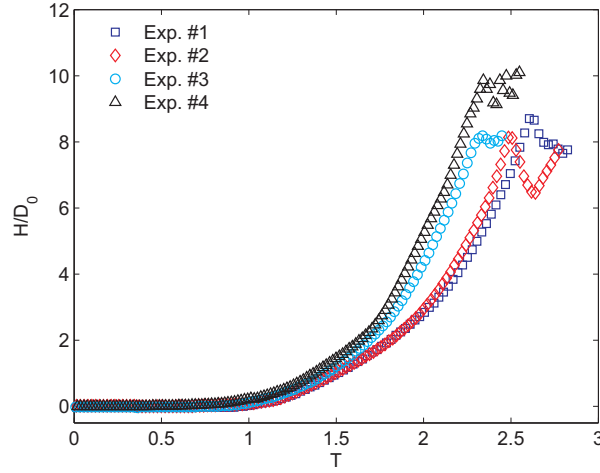


**Figure 6.** Position of the bag tip

The solution of (4) is

$$t = C_1 + \frac{\sqrt{\pi}}{C_2 U_a \sqrt{2}} \sqrt{\frac{\rho_l}{\rho_a}} \operatorname{erfi}[\sqrt{\ln(C_2 R)}], \quad (5)$$

which is an implicit formulation of  $R(t)$  that can be solved numerically. In equation (5),  $C_1$  and  $C_2$  are constants,  $\operatorname{erfi}(\cdot)$  is the imaginary error function. If we assume the initial conditions in the form  $R = D_0/2$  and  $\dot{R} = 0$  at  $t = 0$  (which is justifiable from Fig. 5(b)) expression (5) yields

$$t = \frac{D_0 \sqrt{\pi}}{2\sqrt{2} U_a} \sqrt{\frac{\rho_l}{\rho_a}} \operatorname{erfi}[\sqrt{\ln(2R/D_0)}], \quad (6)$$

At large times the thickness of the disc  $h$  can be roughly estimated from the mass balance of the drop

$$h \approx D_0^3 / (6R^2). \quad (7)$$

It should be noted, that the motion of the disc edge is influenced by the capillary forces leading to formation of the rim, whose relative velocity can be estimated using the expression for the Taylor rim velocity

$$V_R = \sqrt{\frac{2\sigma}{\rho_l h}}. \quad (8)$$

Therefore, the apparent radius  $R_R$  of the disc can be roughly estimated using  $R_R = R - M$ , where  $\dot{M} \approx V_R$ , which is valid if  $M \ll R$ . Expressions (6) and (8) yield

$$R_R \approx R - t \sqrt{\frac{3\sigma}{2D_0 \rho_l}}. \quad (9)$$

### Bag formation

Let us estimate the formation of the bag. The coordinate of the tip of the bag can be estimated from the axial balance of the element of the film

$$\ddot{H} = \frac{p_0}{\rho_l h}, \quad (10)$$

where  $H$  is the axial coordinate of the bag tip (along the air flow direction). We can rewrite (10), using  $R$  as an independent variable, instead of  $t$ . With the help of (6) equation (10) yields

$$H'(R) + 2H''(R)R \ln \frac{2R}{D_0} = \frac{3R^3}{D_0^3}, \quad (11)$$

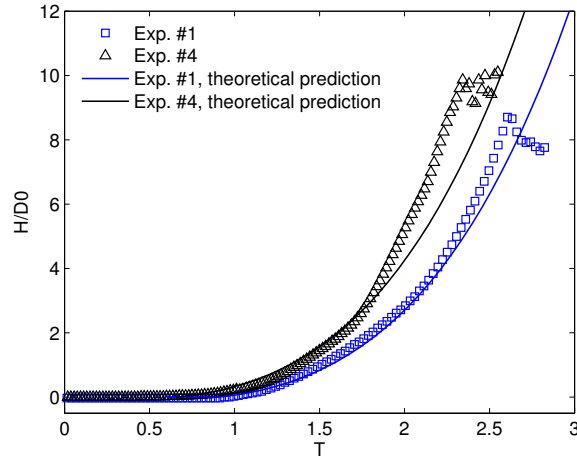


**Figure 7.** Position of the bag tip. Comparison between experimental data (symbols) and theoretical predictions (solid lines).

where the dash denotes differentiation with respect to  $R$ . Equation 11 has to be solved subject the initial conditions  $H(D_0/2) = H'(D_0/2) = 0$ . It can be written in the dimensionless form:

$$\overline{H}'(\overline{R}) + 2\overline{H}''(\overline{R})\overline{R}\ln[2\overline{R}] = 3\overline{R}^3, \quad (12)$$

where the overbared properties are dimensionless, scaled by  $D_0$ .

Equation (11) is singular at  $\overline{R} = 1/2$ . Initially, the radius  $R$  can be assumed in the form  $\overline{R} = 1/2 + \varepsilon$ , where  $\varepsilon$  is small. Linearizing (11) for small  $\varepsilon$  yields

$$\varepsilon\overline{H}''(\varepsilon) + \overline{H}'(\varepsilon) - \frac{9\varepsilon}{4} - \frac{3}{8} = 0. \quad (13)$$

Its solution, satisfying the initial conditions is

$$\overline{H}_{init} = \frac{3\varepsilon}{8} + \frac{9\varepsilon^2}{32}, \quad \overline{H}'_{init} = \frac{3}{8} + \frac{9\varepsilon}{16} \quad (14)$$

Equation (12) is an ordinary differential equation, which can be solved subject the initial conditions:

$$\overline{H}(\overline{R} = 1/2 + \varepsilon) = \overline{H}_{init}, \quad \overline{H}'(\overline{R} = 1/2 + \varepsilon) = \overline{H}'_{init}, \quad (15)$$

Any small  $\varepsilon > 0$  can be chosen for calculations.

A standard Runge-Kutta algorithm is used for solving equation (12). The dependence of the value  $H$  on time is then determined using (6), which again is solved numerically.

A comparison between experimental data and theoretical predictions is depicted in figure 7. The agreement between these is very good. This shows that the balance between inertial forces and the dynamic pressure of the airflow, as described by equation 10, dominates the dynamics of the liquid bag. It is very interesting to note that the influence of surface tension on the bag evolution is rather weak, especially since this study is focused on low Weber number breakup.

Since surface tension and viscosity decrease the growth rate of the liquid bag, the balance between inertial forces and the dynamic pressure alone should overestimate the growth rate of the bag. However, the growth rate is slightly underpredicted by the model presented here. This indicates that either the pressure difference between the two sides of the drop is larger than assumed or that the liquid film thickness on the bag tip is smaller than assumed. This last point might especially be relevant since the liquid film thickness at the bag tip is not only decreased by the growing drop radius, it is also subject to thinning due to the increase in drop length  $L$  (as presented in Fig. 5(a)).

### Summary, Conclusions and Outlook

This study focuses on the investigation of aerodynamic drop fragmentation at low Weber numbers. A new wind tunnel has been designed and manufactured that allows the observation of single bag breakup events. Experiments are conducted at ambient conditions using water and isopropanol as liquids.

A high-speed video system equipped with a high magnification lens is used to record time-resolved shadow-graphs of the breakup process. The series of images have been quantitatively analyzed by an image processing algorithm, able to track the droplet and revealing information about the temporal evolution of the liquid bag. It is shown that the accuracy of the image processing algorithm is very good, so that even small changes in the experimental parameters can be resolved in the results.

Data is presented for the temporal evolution of drop length in airflow direction and the drop radius perpendicular to the airflow direction. The results are shown in a non-dimensional form so that they can easily be used for comparison with and validation of numerical simulations.

A theoretical model is presented that describes the motion of the bag tip in dependence of the Weber number and the density ratio between liquid and gas phase. The model is able to predict the experimental results with good accuracy for the conditions considered in this study. The governing equations of the model are based on the balance between inertial and aerodynamic forces. It is shown that this balance is the main mechanism for the bag tip motion. However, for a more accurate description of the liquid bag dynamics, surface tension and viscosity corrections will be included in the future. In order to validate the model for a wider range of operating parameters, experiments at higher  $We$  numbers will be conducted.

Since the computational cost for the theoretical model is very low, it can be used to compute the dynamics of not only single drops but complete sprays. However, in order to obtain information about the outcome of breakup events, the link between liquid film thickness, diameter of the rim at the moment of rupture and the resulting drop sizes will need to be made.

### Acknowledgements

The authors would like to thank the German Research Foundation (DFG) for funding this study in the framework of the project SFB 568.

### References

- [1] Geppert, S., Guildenbecher, D., Koch, R. and Bauer, H.-J. *Proc. 23th European Conference on Liquid Atomization and Spray Systems, Brno, Czech Republic, 2010.*
- [2] Opfer, L., Roisman, I.V., Tropea, C. *Proc. 24th European Conference on Liquid Atomization and Spray Systems, Estoril, Portugal, 2011.*
- [3] Kelkar, M., Heberlein, J., *Plasma Chemistry and Plasma Processing* 22-1:1-25 (2002).
- [4] Villermaux, E., Bossa, B. *Nature Physics* 5-9:697-702 (2009).
- [5] Guildenbecher, D.R., López-Rivera, C. and Sojka, P.E., *Experiments in Fluids* 46-3:371-402 (2009).
- [6] Theofanous, T.G., *Annual Review of Fluid Mechanics* 43-1:661-690 (2011).
- [7] Hsiang, L.-P., Faeth, G.M. *International Journal of Multiphase Flow* 18-5:635-652 (1992).
- [8] Pilch, E., Erdman, C.A., *International Journal of Multiphase Flow* 13-6:741-757 (1987).
- [9] Theofanous, T.G., Li, G.J., Dinh, T.N. *Journal of Fluids Engineering* 126-4:516-528 (2004).
- [10] Lopez-Rivera, C., Sojka, P.E. *Proc. 22th European Conference on Liquid Atomization and Spray Systems, Como Lake, Italy, 2008.*
- [11] Joseph, D.D., Belanger, J., Beavers G.S. *International Journal of Multiphase Flow* 25-6:1263-1303 (1999).
- [12] Theofanous, T.G., Li, G. *Physics of Fluids* 20-5:052103 (2008).
- [13] Flock, A., Guildenbecher, D.R., Chen, J., Sojka, P.E., Bauer, H.-J. *Proc. 24th European Conference on Liquid Atomization and Spray Systems, Estoril, Portugal, 2011.*